# Strong higher-order angular dependence of spin-orbit torque in W/CoFeB bilayer

Eun-Sang Park,[1,2,*] Dong-Kyu Lee,[3,*] Fei Xue,[4,5] Byoung-Chul Min,[2] Hyun Cheol Koo,[1,2] Paul M. Haney,[4] Kyoung-Whan Kim,[2,†] and Kyung-Jin Lee[6,‡]

[1]*KU-KIST Graduate School of Converging Science and Technology, Korea University, Seoul 02841, Korea*
[2]*Center for Spintronics, Korea Institute of Science and Technology, Seoul 02792, Korea*
[3]*Department of Materials Science and Engineering, Korea University, Seoul 02841, Korea*
[4]*Physical Measurement Laboratory, National Institute of Standards and Technology, Gaithersburg, Maryland 20899, USA*
[5]*Department of Physics, University of Alabama at Birmingham, Birmingham, Alabama 35294, USA*
[6]*Department of Physics, Korea Advanced Institute of Science and Technology (KAIST), Daejeon 34141, Korea*

(Dated: March 15, 2023)

The symmetry of normal metal/ferromagnet bilayers allows spin-orbit torques (SOTs) to simultaneously have two distinct angular dependences on the magnetization direction $\hat{\mathbf{m}}$. The most well-studied forms of SOT consist of the conventional fieldlike and dampinglike torques, which we label as "lowest-order" SOT. There are additional SOT forms associated with spin polarization different from that of the lowest-order SOT, and which contain an extra factor of $\hat{\mathbf{m}}$-dependence. We label these as "higher-order" SOT. Understanding SOT-driven magnetization dynamics requires detailed information about the full angular dependence. In this work, we measure both the lowest-order and higher-order angular dependences of SOTs in three types of bilayer, Pt/Co, Ta/CoFeB, and W/CoFeB, using harmonic Hall measurement. It is found that the higher-order SOT is negligible for Pt/Co and Ta/CoFeB, whereas it is dominant over the lowest-order one for W/CoFeB. Macrospin simulations show that the higher-order SOT can significantly affect magnetization dynamics, which is qualitatively in line with SOT-induced switching experiments.

## I. INTRODUCTION

In-plane current-induced spin-orbit torque (SOT) in normal metal/ferromagnet bilayers has attracted interest due to its capability to switch the magnetization [1, 2], to induce magnetization oscillation [3], and to move magnetic textures such as domain walls [4, 5] and skyrmions [6, 7]. This versatility of SOT has motivated researchers to investigate various origins of SOT [8–35, 37–53] and to develop SOT-active devices [54–72].

In normal metal/ferromagnet bilayers with continuous rotation symmetry about the stacking axis, the magnetization-dependence of the SOT is constrained by symmetry [22, 47, 48]. We can partition the total SOT $\boldsymbol{\tau}$ as a sum of two terms $\boldsymbol{\tau}_1$ and $\boldsymbol{\tau}_2$ with distinct angular dependences [48]:

$$\boldsymbol{\tau}_1 = \gamma \sum_{l=0}^{\infty} m_z^{2l} [a_l \mathbf{p} \times \hat{\mathbf{m}} + b_l \hat{\mathbf{m}} \times (\mathbf{p} \times \hat{\mathbf{m}})], \quad (1)$$

$$\boldsymbol{\tau}_2 = \gamma \sum_{l=0}^{\infty} m_z^{2l} (\hat{\mathbf{m}} \cdot \hat{\mathbf{E}}) [c_l \hat{\mathbf{z}} \times \hat{\mathbf{m}} + d_l \hat{\mathbf{m}} \times (\hat{\mathbf{z}} \times \hat{\mathbf{m}})]. \quad (2)$$

Here $\gamma$ is the gyromagnetic ratio, $m_z = \hat{\mathbf{m}} \cdot \hat{\mathbf{z}}$, $\hat{\mathbf{m}}$ is the magnetization direction, $\hat{\mathbf{z}}$ is the direction normal to the film plane, $\mathbf{p} = \hat{\mathbf{z}} \times \hat{\mathbf{E}}$, $\hat{\mathbf{E}}$ is the electric-field direction, and $a_l$, $b_l$, $c_l$, and $d_l$ are effective spin-orbit magnetic fields for corresponding SOT vectors. We note that Eqs. (1) and (2) are equivalent to SOT equations of Ref. [22] when including all higher-order terms.

Note that $\boldsymbol{\tau}_2$ contains an additional factor of $\hat{\mathbf{m}}$ compared to $\boldsymbol{\tau}_1$, so we refer to $\boldsymbol{\tau}_2$ as "higher-order" SOT, and $\boldsymbol{\tau}_1$ as "lowest-order" SOT. The lowest-order torque [Eq. (1)] is associated with spin polarization in $\mathbf{p}$, which is $\hat{\mathbf{y}}$ for $\hat{\mathbf{E}} = \hat{\mathbf{x}}$, and consists of the conventional dampinglike [$\propto b_l \hat{\mathbf{m}} \times (\mathbf{p} \times \hat{\mathbf{m}})$] and fieldlike [$\propto a_l \mathbf{p} \times \hat{\mathbf{m}}$] torques. On the other hand, the higher-order torque [Eq. (2)] is distinct from the lowest-order one as it is associated with spin polarization in $\hat{\mathbf{z}}$ and is proportional to $(\hat{\mathbf{m}} \cdot \hat{\mathbf{E}})$. Although the higher-order SOT has been identified in experiments [22, 67] and first-principles calculation [47], most SOT experiments up to now have been analyzed based on the lowest-order one. However, the higher-order angular dependence as well as the lowest-order one is important to understand SOT-driven magnetization dynamics [48, 59]. For instance, an in-plane magnetic field is usually applied in the direction of $\hat{\mathbf{E}}$ for deterministic SOT switching of perpendicular magnetization [1]. This in-plane field makes the $(\hat{\mathbf{m}} \cdot \hat{\mathbf{E}})$ term of Eq. (2) non-zero so that the higher-order torque is active even at the initial stage of SOT switching dynamics. In this respect, the higher-order SOT must be investigated in various normal metal/ferromagnet bilayers.

In this work, we measure both the lowest-order and higher-order angular dependences of SOT in three types of normal metal/ferromagnet bilayer, Pt/Co, Ta/CoFeB, and W/CoFeB, using the harmonic Hall measurement [14, 16, 22, 46]. Among the three bilayers, only W/CoFeB is found to exhibit a significant higher-order SOT. Macrospin simulations show that the switching current significantly depends on the higher-order torque, which is qualitatively consistent with SOT switching experiments.

* These two authors contributed equally to this work.
† kwk@kist.re.kr
‡ kjlee@kaist.ac.kr

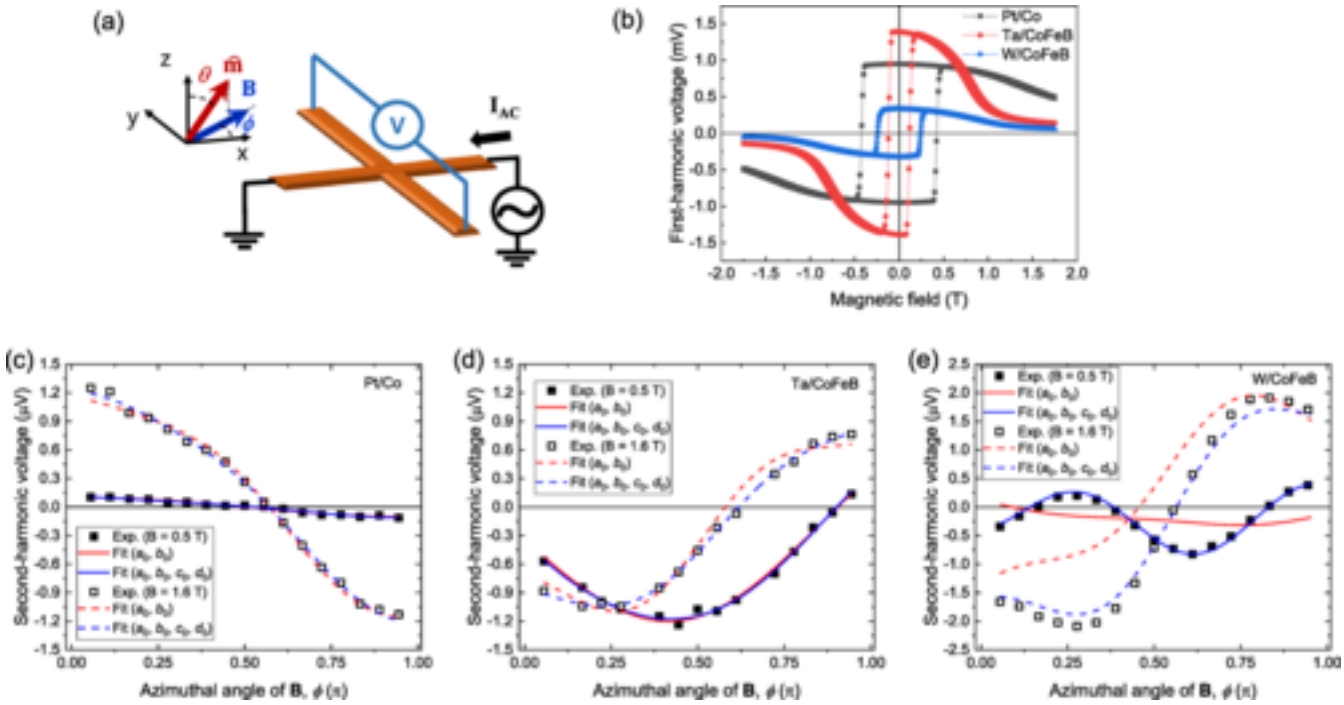


FIG. 1. (color online) (a) A schematic diagram of harmonic Hall measurement. Here $I_{\rm AC}$ is the injected AC current at frequency of 401 Hz, $V$ is the measured Hall voltage, $\mathbf{B}$ is the external magnetic field, and $\theta$ and $\phi$ are the polar and azimuthal angles of the magnetization $\hat{\mathbf{m}}$, respectively. The azimuthal angle $\phi$ is same for $\hat{\mathbf{m}}$ and $\mathbf{B}$. (b) The first-harmonic signals for Pt/Co, Ta/CoFeB, and W/CoFeB. The second-harmonic signals of (c) Pt/Co, (d) Ta/CoFeB, and (e) W/CoFeB at $|\mathbf{B}| = 0.5$ T and 1.6 T. In (c)–(e), symbols are experimental results and red (blue) curves are fitting results with only $a_0$ and $b_0$ (with all of $a_0$, $b_0$, $c_0$, and $d_0$) The polar angles (radians) of the magnetization are: (c) 0.2844 for $|\mathbf{B}| = 0.5$ T and 0.9704 for $|\mathbf{B}| = 1.6$ T, (d) 0.6530 for $|\mathbf{B}| = 0.5$ T and 1.4624 for $|\mathbf{B}| = 1.6$ T, and (e) 0.6131 for $|\mathbf{B}| = 0.5$ T and 1.4284 $|\mathbf{B}| = 1.6$ T.

## II. EXPERIMENTAL RESULTS

We fabricate three types of sample, Ta (5 nm)/Pt (3 nm)/Co (1 nm)/CAP, Ta (5 nm)/$Co_4Fe_4B_2$ (0.9 nm)/CAP, and W (5 nm)/$Co_4Fe_4B_2$ (1 nm)/CAP, where the CAP is MgO (2 nm)/Ta (2 nm), using magnetron sputtering at a base pressure of low $10^{-6}$ Pa ($10^{-8}$ Torr). Pt, Ta, W, Co, and CoFeB layers are deposited at Ar pressure of 0.133 Pa (1 mTorr) and MgO layer at 0.533 Pa (4 mTorr). The samples are annealed at 350 °C (Pt/Co, W/CoFeB) or 280 °C (Ta/CoFeB), to achieve perpendicular magnetic anisotropy. The samples are patterned into Hall bars (Hall cross area of $5 \times 5$ $\mu$m$^2$) by photolithography and ion milling. We measure first- and second-harmonic signals as a function of magnetic field $\mathbf{B}$ at various azimuthal angles $\phi$ with a lock-in amplifier. The polar angle of the magnetic field is about 85°. A schematic diagram of the harmonic Hall measurement is shown in Fig. 1(a). We measure the saturation magnetization $M_{\rm S}$, the effective perpendicular anisotropy field $B_{\rm an}$, and the coercivity $B_c$ (see Table I) using the vibrating sample magnetometer (VSM) (see Fig. 5 in the Appendix) and the first-harmonic Hall signals. We also measure resistivities of heavy metal layers [Pt (3 nm), Ta (5 nm), W (5 nm)] using the four-probe measurement ($\rho_{\rm Pt} = 49\mu\Omega\cdot$cm, $\rho_{\rm Ta} = 176\mu\Omega\cdot$cm, $\rho_{\rm W} = 180\mu\Omega\cdot$cm). The resistivities of Ta and W suggest that they are in the $\beta$ phase.

In harmonic Hall measurements [14, 16, 22, 46], the first-harmonic signal represents the equilibrium magnetization direction whereas the second-harmonic signal represents the perturbative magnetization tilting induced by SOT. The polar angle $\theta$ of the magnetization is maintained to be the same at different azimuthal angles of $\mathbf{B}$ by carefully monitoring the first-harmonic signals. The anomalous Nernst and planar Hall contributions are corrected from the second-harmonic signals [22, 46]. The ratio $r_{\rm H}$ of planar Hall resistance to anomalous Hall resistance for each bilayer is shown in Table I. We note that the W/CoFeB exhibits the largest planar Hall effect. We will get back to this in the summary section.

We fit the second-harmonic signals based on the following

TABLE I. Properties of three types of bilayer: Effective perpendicular anisotropy field ($B_{\rm an}$), coercivity ($B_c$), saturation magnetization ($M_{\rm S}$), ratio of planar Hall resistance to anomalous Hall resistance ($r_{\rm H}$), and switching efficiencies for single-domain switching ($R_{\rm SD}$) and domain-wall switching ($R_{\rm DW}$).

| | $B_{\rm an}$ (T) | $B_c$ (mT) | $M_{\rm S}$ (kA/m) | $r_{\rm H}$ | $R_{\rm SD}$ ($\times 10^{-11}$T·m$^2$) | $R_{\rm DW}$ ($\times 10^{-12}$T·m$^2$) |
|---|---|---|---|---|---|---|
| Pt/Co | 1.74 | 58.55 | 1228 | 0.47 | 3.41 | 1.16 |
| Ta/CoFeB | 0.78 | 3.25 | 742 | 0.23 | 2.46 | 0.10 |
| W/CoFeB | 0.85 | 6.84 | 773 | 2.85 | 3.45 | 0.29 |

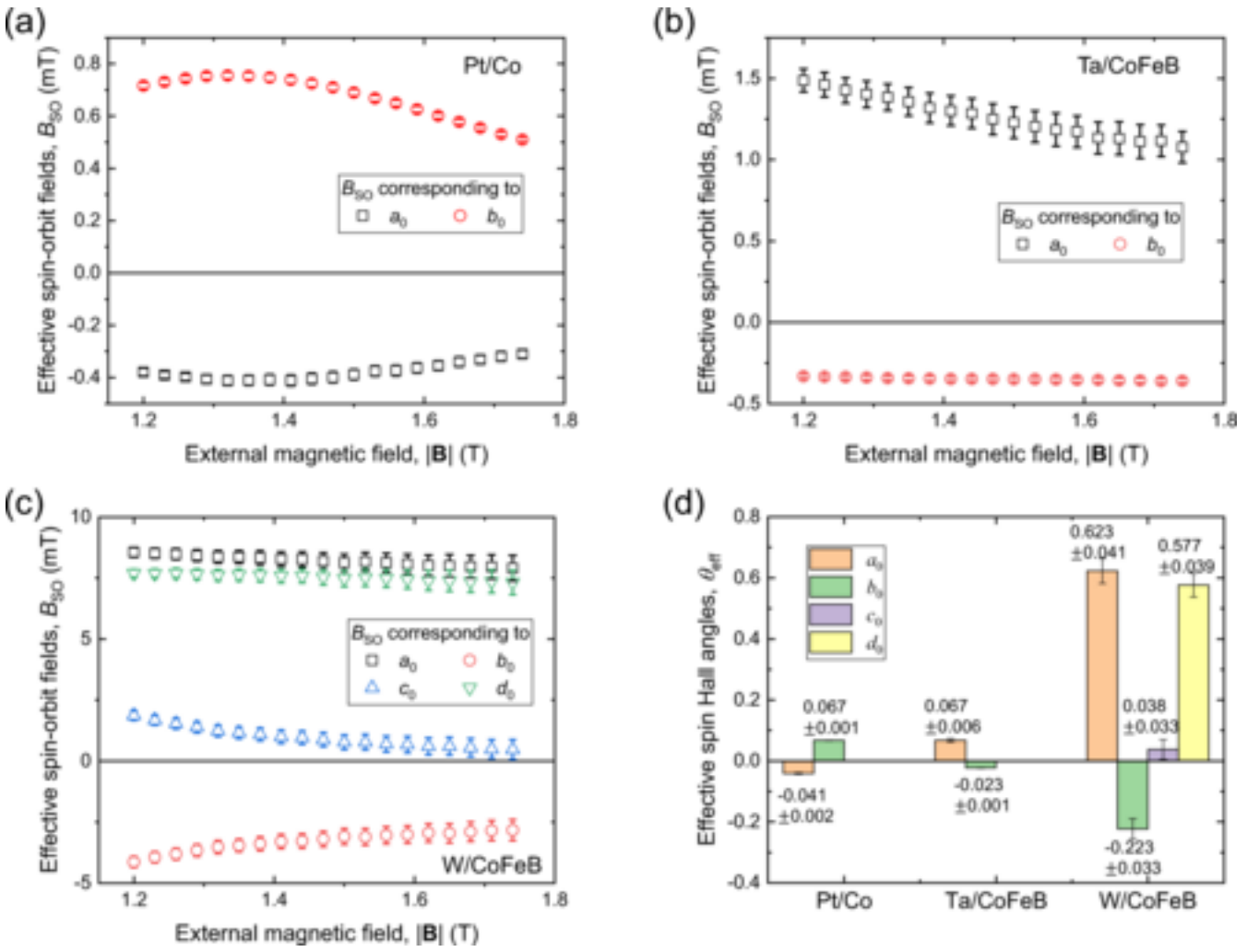


FIG. 2. (color online) Effective spin-orbit fields $B_{\rm SO}$ as a function of the external magnetic field $|\mathbf{B}|$ in the high field regime: (a) Pt/Co, (b) Ta/CoFeB, and (c) W/CoFeB. (d) Effective spin Hall angles $\theta_{\rm eff}$ corresponding to $a_0$, $b_0$, $c_0$, and $d_0$ for the three types of bilayer. All error bars indicate single-standard-deviation uncertainties. The AC current magnitude is 1 mA.

torque equation:

$$\begin{aligned}\frac{\boldsymbol{\tau}}{\gamma} &= a_0\hat{\mathbf{y}}\times\hat{\mathbf{m}} + b_0\hat{\mathbf{m}}\times(\hat{\mathbf{y}}\times\hat{\mathbf{m}}) \\ &+ (\hat{\mathbf{m}}\cdot\hat{\mathbf{x}})[c_0\hat{\mathbf{z}}\times\hat{\mathbf{m}} + d_0\hat{\mathbf{m}}\times(\hat{\mathbf{z}}\times\hat{\mathbf{m}})].\end{aligned} \tag{3}$$

It is noted that Eq. (3) corresponds to the terms corresponding to $l = 0$ of the lowest-order SOT [i.e., Eq. (1); $a_0$ and $b_0$] and the higher-order SOT [i.e., Eq. (2); $c_0$ and $d_0$]. This choice minimizes the number of fitting parameters (i.e., $a_0$, $b_0$, $c_0$, and $d_0$). From Eq. (3), we obtain the following angle-dependent second-harmonic Hall voltage $V_{2\omega}^{\rm fit}$ for fitting the experimental result:

$$\begin{aligned}V_{2\omega}^{\rm fit} &= V_{\rm AH}\frac{A_2}{A_1} \\ &- V_{\rm PH}\left(\frac{A_2}{A_1}\cos\theta\sin 2\phi + \frac{A_4}{A_3}\sin\theta\cos\phi\cos 2\phi\right), \\ A_1 &= 2[B_{\rm an}\cos 2\theta + B_0\cos(\theta-\theta_H)], \\ A_2 &= (2b_0 + c_0 - c_0\cos 2\theta)\cos\phi - 2a_0\cos\theta\sin\phi, \\ A_3 &= B_{\rm an}\cos\theta + B_0\cos\theta_H, \\ A_4 &= -d_0\cos\theta\sin\theta + \cot\theta(a_0 + b_0\cos\theta\tan\phi),\end{aligned} \tag{4}$$

where the magnetization $\hat{\mathbf{m}} = (\cos\phi\sin\theta, \sin\phi\sin\theta, \cos\theta)$, the external field $\mathbf{B} = B_0(\cos\phi\sin\theta_H, \sin\phi\sin\theta_H, \cos\theta_H)$, and $V_{\rm AH}$ ($V_{\rm PH}$) is the anomalous (planar) Hall voltage. We obtain $B_{\rm an}$ and $\theta_H$ by analyzing the first-harmonic signal with respect to $B_0$. We note that unconventional SOTs originating from symmetry breaking [33–36, 38–40] causes an additional angular dependence of the second-harmonic signal that is not allowed by the lowest-order SOT [i.e., $a_0$- and $b_0$-related

terms in Eq. (3)]. However, the additional angular dependence from unconventional SOTs is clearly different from that of the higher-order SOTs in this work [i.e., $c_0$- and $d_0$-related terms in Eq. (3)]. For instance, the lateral symmetry breaking [33–35] or the time-reversal symmetry breaking using magnetism [38–40] induces spin currents carrying the $z$ polarization. The higher-order term in Eq. (3) contains an additional factor of $(\hat{\mathbf{m}} \cdot \hat{\mathbf{x}})$ as compared to the unconventional SOT originating from $z$-spin currents so that they result in clearly different angular dependences of the second-harmonic Hall signals.

Representative second-harmonic signals as a function of the azimuthal angle $\phi$ of $\mathbf{B}$ for three types of bilayer are shown in Fig. 1(b)–(d), where symbols are experimental results. We fit the experimental results with only $a_0$ and $b_0$ (red curves) and with all of $a_0$, $b_0$, $c_0$ and $d_0$ (blue curves). At both intermediate ($|\mathbf{B}| = 0.5$ T) and high ($|\mathbf{B}| = 1.6$ T) magnetic fields, the second-harmonic signals of Pt/Co and Ta/CoFeB are reasonably fitted with only $a_0$ and $b_0$ (i.e., only lowest-order angular dependence or, equivalently, only conventional fieldlike and dampinglike torques). In contrast, the second-harmonic signals of W/CoFeB cannot be fitted with only $a_0$ and $b_0$. On the other hand, when we fit with all of $a_0$, $b_0$, $c_0$ and $d_0$ (blue curves), we obtain a reasonable fitting even for W/CoFeB. This tendency is found to be valid for full angle ranges from 0 to $2\pi$ (not shown) so that it is not an artifact from possible thermoelectric signals. [73] These results show that the higher-order angular dependence of SOT (i.e., $c_0$ and $d_0$) is strong for W/CoFeB, whereas it is weak for Pt/Co and Ta/CoFeB. This weak higher-order angular dependence for Pt/Co and Ta/CoFeB is inconsistent with the results of Ref. [22]. Moreover, the strong higher-order angular dependence for W/CoFeB is also inconsistent with previous studies [74, 75] showing that the second-harmonic Hall signals in W/CoFeB bilayers can be well analyzed by using the conventional SOT model without considering any higher-order SOT terms. We attribute this inconsistency to the difference in detailed sample structures, i.e., different thickness, capping layer, and annealing temperature.

Figure 2 shows the fitting result of the second-harmonic signal as a function of the external magnetic field $|\mathbf{B}|$ in the high field regime ($|\mathbf{B}| > 1.2$ T). We here focus on the high field regime to make $(\hat{\mathbf{z}} \times \hat{\mathbf{m}})$ large, in order to reliably fit the coefficients of higher-order SOT, $c_0$ and $d_0$ [see Eq. (3)]. We plot effective spin-orbit fields $B_{\rm SO}$, i.e., fitted $a_0$, $b_0$, $c_0$, and $d_0$. For Pt/Co [Fig. 2(a)] and Ta/CoFeB [Fig. 2(b)], we present fitting results with only $a_0$ and $b_0$ because they reasonably fit the second-harmonic signals. For W/CoFeB [Fig. 2(c)], on the other hand, we present the fitting results with all of $a_0$, $b_0$, $c_0$ and $d_0$. All fitting results of Fig. 2(a)–(c) have relatively small error bars.

Several features of $B_{\rm SO}$ are as follows: First, $b_0$, which corresponds to the conventional dampinglike torque, is positive for the Pt/Co [Fig. 2(a)], whereas it is negative for the Ta/CoFeB [Fig. 2(b)] and W/CoFeB [Fig. 2(c)]. The sign of $b_0$ is consistent with the established sign of the spin Hall angle of the normal metal (Pt, Ta, and W). Second, for all three bilayers, $a_0$ and $b_0$ (or $a_0$, $b_0$, $c_0$, and $d_0$) exhibit some variations with the external magnetic field $|\mathbf{B}|$, thus the polar angle $\theta$. This polar-angle dependence suggests that the SOT terms corresponding to $l > 0$ of Eqs. (1) and (2) are still effective even in the high field regime. Third, in case of W/CoFeB, $c_0$ is small but $d_0$ is large and even larger in magnitude than $b_0$.

In Fig. 2(d), we summarize effective spin Hall angles $\theta_{\rm eff}$ corresponding to $a_0$, $b_0$, $c_0$, and $d_0$. $\theta_{\rm eff}$ is calculated from $2eM_{\rm S}t_{\rm F}B_{\rm SO}/\hbar J$ at $|\mathbf{B}| = 1.74$ T, where $e$ is the electron charge, $M_{\rm S}$ is the saturation magnetization of ferromagnet, $t_{\rm F}$ is the thickness of ferromagnet, $\hbar$ is the reduced Planck constant, and $J$ is the current density flowing through a relevant heavy metal layer, which is estimated with considering current distributions due to different resistivities and thicknesses. For the resistivity, we use measured results for heavy metals (Pt, Ta , W) and literature values for Co ($\rho_{\rm Co} = 20\mu\Omega \cdot {\rm cm}$ [76]) and for CoFeB ($\rho_{\rm CoFeB} = 130\mu\Omega \cdot {\rm cm}$ [77]). We find that $a_0$ and $b_0$ of W/CoFeB are much larger in magnitude than those of Pt/Co and Ta/CoFeB. In addition, W/CoFeB exhibits a large $d_0$, which is a coefficient of a higher-order SOT $\propto (\hat{\mathbf{m}} \cdot \hat{\mathbf{x}})\hat{\mathbf{m}} \times (\hat{\mathbf{z}} \times \hat{\mathbf{m}})$. This strong higher-order angular dependence of SOT for W/CoFeB suggests that the SOT-driven magnetization dynamics of this bilayer is substantially different from other two bilayers.

To get insight into how the strong higher-order SOT (i.e., $d_0$) affects the magnetization dynamics of W/CoFeB, we carry out switching experiments with a pulsed current (pulse width $= 100$ $\mu$s) in the presence of an in-plane field $B_x$. The switching polarity is found to be consistent with the sign of $b_0$, the conventional dampinglike torque (not shown). Figure 3(a) shows the switching current as a function of $B_x$ for the three bilayers. The switching current decreases with $B_x$ for Ta/CoFeB and W/CoFeB, whereas it is almost constant for Pt/Co because of its large anisotropy field (Table I). Assuming that only $b_0$ is non-zero while all of $a_0$, $c_0$, and $d_0$ are zero, a SOT switching efficiency $\mathcal{R}_{\rm SD}$ for the single-domain switching can be defined as $\mathcal{R}_{\rm SD} = (B_{\rm an} - \sqrt{2}B_x)M_{\rm S}t_{\rm F}/J_{\rm SW}$ [55] and a SOT switching efficiency $\mathcal{R}_{\rm DW}$ for the domain-wall switching can be defined as $\mathcal{R}_{\rm DW} = B_c M_{\rm S} t_{\rm F}/J_{\rm SW}$ [52], where $J_{\rm SW}$ is the switching current density. From the measured $J_{\rm SW}$ at $B_x = 10$ mT, we estimate $\mathcal{R}_{\rm SD}$ and $\mathcal{R}_{\rm DW}$ for the three bilayers [Fig. 3(b); Table I]. For $\mathcal{R}_{\rm DW}$, which is relevant to the large sample used in this work, the SOT switching efficiency is the largest for the Pt/Co and the smallest for the Ta/CoFeB.

It is interesting to observe that the SOT switching efficiencies are uncorrelated with $b_0$: The W/CoFeB exhibits a much larger $b_0$ than the Pt/Co. This indicates that the conventional dampinglike torque ($b_0$) does not solely determine the switching current but other torque components also contribute to the switching current. Considering the conventional fieldlike SOT ($a_0$) does not improve the correlation. The ratio $b_0/a_0$ is similar for W/CoFeB and Ta/CoFeB, but the magnitudes of $a_0$ and $b_0$ are different by an order of magnitude. Therefore, if the conventional SOTs ($a_0$ and $b_0$) determine the switching current, the switching efficiencies of W/CoFeB must be larger than those of Ta/CoFeB by an order of magnitude. However, the switching efficiencies do not show such a large difference [Fig. 3(b); Table I], suggesting that the large positive $d_0$ of W/CoFeB may increase the switching current density significantly. We note that a similar uncorrelation between the effec-

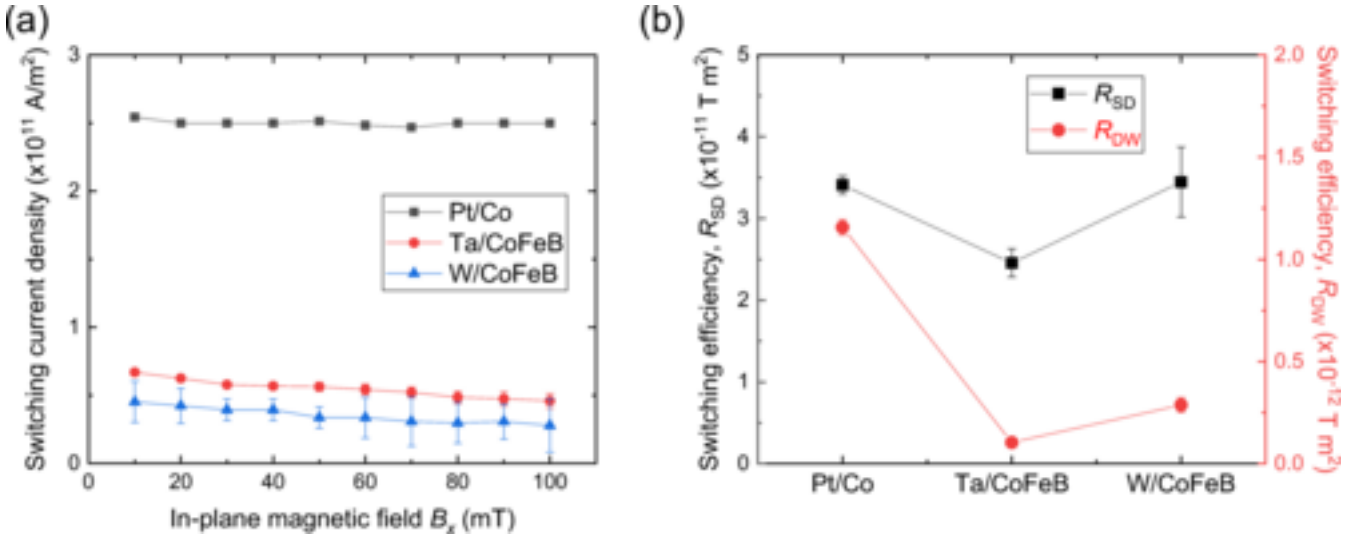


FIG. 3. (color online) SOT switching experiment: (a) The switching current density as a function of an in-plane field $B_x$. (b) Switching efficiencies for the single-domain switching ($\mathcal{R}_{\rm SD}$) and for the domain-wall switching ($\mathcal{R}_{\rm DW}$), which are defined in the main text.

tive spin Hall angles corresponding to the lowest-order SOT and the SOT switching efficiencies was recently reported [52], but the role of the higher-order SOT in the uncorrelation was not investigated.

## III. MACROSPIN SIMULATION RESULTS

To understand the effect of higher-order SOT corresponding to $d_0$ on the magnetization switching, we carry out macrospin simulations based on the Landau-Lifshitz-Gilbert (LLG) equation including both the lowest-order and higher-order SOTs:

$$\begin{aligned}\frac{d\hat{\mathbf{m}}}{dt} = &- \gamma\hat{\mathbf{m}}\times(B_{\rm an}\hat{\mathbf{z}}+B_x\hat{\mathbf{x}})+\alpha\hat{\mathbf{m}}\times\frac{d\hat{\mathbf{m}}}{dt} \\ &+ \gamma a_0\hat{\mathbf{y}}\times\hat{\mathbf{m}}+\gamma b_0\hat{\mathbf{m}}\times(\hat{\mathbf{y}}\times\hat{\mathbf{m}}) \\ &+ \gamma(\hat{\mathbf{m}}\cdot\hat{\mathbf{x}})[d_0\hat{\mathbf{m}}\times(\hat{\mathbf{z}}\times\hat{\mathbf{m}})].\end{aligned} \quad (5)$$

Here, $\alpha$ is the damping constant, $a_0(b_0) = \hbar\theta_{{\rm eff},a_0(b_0)}J/2eM_{\rm S}t_{\rm F}$ is the lowest-order spin-orbit field, $d_0 = \hbar\theta_{{\rm eff},d_0}J/2eM_{\rm S}t_{\rm F}$ is the higher-order spin-orbit field, and $\theta_{{\rm eff},i}$ ($i = a_0, b_0, d_0$) is the effective spin Hall angle corresponding to each torque component. The higher-order SOT corresponding to $c_0$ is not included in Eq. (5) because $c_0$ is negligible or much smaller than other torque components in experiments [Fig. 2(d)].

Figure 4(a) and 4(b) show simulated switching phase diagrams as functions of the current density $J$ and the higher-order torque corresponding to $\theta_{{\rm eff},d_0}$. The color code represents the $m_z$ component while the current is on. As the initial magnetization is set along $+\hat{\mathbf{z}}$, the (light) blue region corresponds to the switching, whereas the (light) red region corresponds to the not-switching. Figure 4(a) shows a switching phase diagram for $\theta_{{\rm eff},a_0} = 0$ and $\theta_{{\rm eff},b_0} = -0.2$ (thus, only $b_0$ and $d_0$ are non-zero). For a negative $\theta_{{\rm eff},d_0}$, the switching current density $J_{\rm SW}$ decreases with $|\theta_{{\rm eff},d_0}|$. For a positive $\theta_{{\rm eff},d_0}$, on the other hand, $J_{\rm SW}$ rapidly increases with $\theta_{{\rm eff},d_0}$.

This dependence of $J_{\rm SW}$ on the sign of $\theta_{{\rm eff},d_0}$ can be understood as follows. The in-plane magnetic field $B_x(>0)$ makes the magnetization tilt towards $+\hat{\mathbf{x}}$ direction [see Fig. 4(c) and 4(d)] so that $(\hat{\mathbf{m}}\cdot\hat{\mathbf{E}})$ is non-zero and the higher-order SOT affects the magnetization dynamics even at the initial time stage. As the higher-order $d_0$ torque is along $\hat{\mathbf{m}}\times(\hat{\mathbf{z}}\times\hat{\mathbf{m}})$, it acts like a spin-transfer torque for a perpendicularly magnetized spin valve in the current-perpendicular-to-plane geometry. As a result, the $d_0$ torque acts as an antidamping or additional damping torque for the $z$-component of magnetization, depending on the sign of $d_0$. For a positive $\theta_{{\rm eff},d_0}$, the $d_0$ torque acts as an additional damping one, so that the switching occurs when there is no static solution of Eq. (5) for $m_z > 0$, corresponding to the instability condition [55]. Figure 4(c) shows time evolution of $\hat{\mathbf{m}}$ for this case where the magnetization follows a simple trajectory with no multiple precessions during the switching. For a negative $\theta_{{\rm eff},d_0}$, on the other hand, the $d_0$ torque acts as an antidamping one, so that the switching occurs when the $d_0$ antidamping torque overcomes the intrinsic damping torque, corresponding to the antidamping condition. Figure 4(d) shows time evolution of $\hat{\mathbf{m}}$ for this case where the magnetization undergoes multiple precessions during the switching.

The analytic expressions for the switching current density are too complicated to obtain because of the proportional factor $(\hat{\mathbf{m}}\cdot\hat{\mathbf{E}})$ of $d_0$ torque. Instead, we obtain $J_{\rm SW}$ numerically by applying the instability (antidamping) condition to Eq. (5) for $\theta_{{\rm eff},d_0} > 0$ ($\theta_{{\rm eff},d_0} < 0$). In Fig. 4(a), yellow and green curves correspond to the numerically obtained switching boundaries for the instability and antidamping conditions, respectively, which are in agreement with the LLG simulation results.

Figure 4(b) shows a switching phase diagram for $\theta_{{\rm eff},a_0} = 0.6$ and $\theta_{{\rm eff},b_0} = -0.2$ [thus, as in the experimental result of W/CoFeB, the conventional fieldlike torque $a_0$ is additionally non-zero in comparison to Fig. 4(a)]. Even with a non-zero $a_0$, the switching phase diagram exhibits qualitatively similar

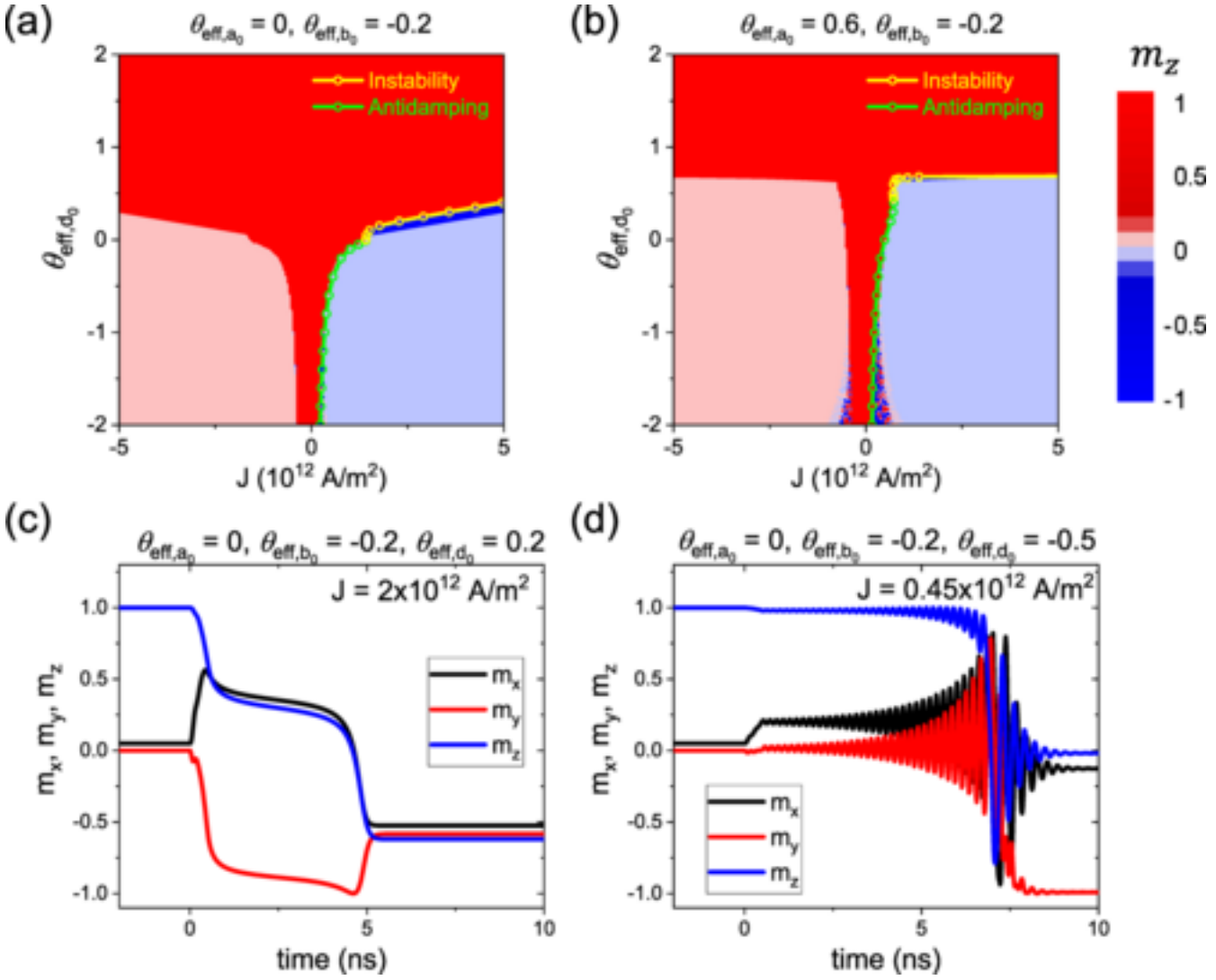


FIG. 4. (color online) Switching phase diagram as functions of the current density $J$ and the higher-order torque corresponding to $d_0$ (i.e., $\theta_{\mathrm{eff},d_0}$) when (a) $(\theta_{\mathrm{eff},a_0}, \theta_{\mathrm{eff},b_0}) = (0.0, -0.2)$ and (b) $(\theta_{\mathrm{eff},a_0}, \theta_{\mathrm{eff},b_0}) = (0.6, -0.2)$. For both (a) and (b), $\theta_{\mathrm{eff},c_0}$ is assumed to be zero. The color code represents the $m_z$ component while the current is on. The (light) blue region corresponds to the switching, whereas the (light) red region corresponds to the not-switching. Yellow and green curves are the switching current densities obtained from the instability and antidamping conditions, respectively. Time evolution of $\hat{\mathbf{m}}$ for (c) $(\theta_{\mathrm{eff},a_0}, \theta_{\mathrm{eff},b_0}, \theta_{\mathrm{eff},d_0}) = (0.0, -0.2, 0.2)$ and (d) $(\theta_{\mathrm{eff},a_0}, \theta_{\mathrm{eff},b_0}, \theta_{\mathrm{eff},d_0}) = (0.0, -0.2, -0.5)$. Other parameters: the effective perpendicular magnetic anisotropy field $B_{\mathrm{K}} = 0.2$ T, the external magnetic field $B_x = 10$ mT, ferromagnet thickness $t_F = 1$ nm, the gyromagnetic ratio $\gamma = 1.76 \times 10^{11}$ T$^{-1}$s$^{-1}$, the saturation magnetization $M_{\mathrm{S}} = 10^3$ kA/m, and the damping constant $\alpha = 0.1$.

features [Fig. 4(b)] and the numerically obtained switching boundaries for the instability and antidamping conditions also reproduce the LLG simulation results. One difference from the switching phase diagram of Fig. 4(a) is that a steady oscillation occurs near the switching boundaries at a large negative $\theta_{\mathrm{eff},d_0}$, which is indicated by red-blue mixed region in Fig. 4(b). We also note that the switching boundary for the instability condition [yellow curve in Fig. 4(b)] looks flat at a large current, but it has a non-zero slope.

The above simulation results show that a negative (positive) $d_0/b_0$ in general increases (decreases) $J_{\mathrm{SW}}$ from that expected without $d_0$ torque. As the W/CoFeB has a negative $d_0/b_0$, the discrepancy between the effective spin Hall angles [$\theta_{\mathrm{eff},i}$ ($i = a_0$, $b_0$, $c_0$, $d_0$)] and the SOT switching efficiencies ($\mathcal{R}_{\mathrm{SD}}$ and $\mathcal{R}_{\mathrm{DW}}$), discussed in the previous section, can be qualitatively explained by the macrospin simulation results.

## IV. SUMMARY

In this work, we measure the lowest-order and higher-order SOTs of Pt/Co, Ta/CoFeB, and W/CoFeB bilayers, using the harmonic Hall measurement. A large higher-order SOT ($d_0$) is observed for the W/CoFeB bilayer. The comparison between the effective spin Hall angles [$\theta_{\mathrm{eff},i}$ ($i = a_0$, $b_0$, $c_0$, $d_0$)], esti-

mated from harmonic Hall measurements, and the SOT switching efficiencies ($\mathcal{R}_{\rm SD}$ and $\mathcal{R}_{\rm DW}$), estimated from switching experiments, implies an important role of the higher-order torque in the SOT-induced switching dynamics. Macrospin simulation shows that depending on the sign of $d_0$, the higher-order $d_0$ torque increases or decreases the switching current, which is qualitatively consistent with experimental results.

Our result suggests that measuring the higher-order torque is of crucial importance for the performance of SOT devices, because a positive large $d_0$ makes the switching extremely difficult whereas a negative $d_0$ reduces the switching current. It also demands a further understanding about the physical origin of higher-order SOTs: What determines the sign and magnitude of higher-order SOTs? Related to this question, an interesting observation in our experiment is that the W/CoFeB exhibits the largest planar Hall effect among the three bilayers (Table I). It implies that the higher-order SOT is possibly related to some mechanisms responsible for the planar Hall effect. Concerning this possibility, we note that the higher-order SOT was called the planar-Hall-like torque in a first-principles study [47] because their angular dependences are similar. However, the planar Hall effect (or transverse anisotropic magnetoresistance effect) itself generates spin currents polarized along the magnetization [27] so that these spin currents are unable to exert SOTs on the magnetization. In this respect, the higher-order SOT is different from the planar Hall torque reported in an experiment [43] where it was argued that the planar Hall effect of a ferromagnet exerts magnon torques on the ferromagnet itself. To understand the origin of higher-order SOT and its possible relation to the planar Hall effect, further experiments and first-principles calculations of the higher-order SOT for various materials must be carried out. Finally, although we ignore the higher-order $c_0$ torque in our analysis because it is found to be small in the tested bilayers, it may be not small in other bilayers so that SOT-induced magnetization dynamics must in general be studied in four-parameter (i.e., $a_0$, $b_0$, $c_0$, $d_0$) space. This four-dimensional phase space would provide a rich phase diagram and associated applications based on SOT-active devices.

## ACKNOWLEDGMENTS

This work was supported by the National Research Foundation of Korea (NRF) funded by the Ministry of Science and ICT (NRF-2020R1A2C3013302, 2022M3H4A1A04096339, 2020R1C1C1012664), the KIST Institutional Program (2E31541,2E31543), the National Research Council of Science and Technology (NST) (CAP-16-01-KIST), and Samsung Electronics Co., Ltd. (IO201019-07699-01). F.X. acknowledges support under the Cooperative Research Agreement between the University of Maryland and the National Institute of Standards and Technology Physical Measurement Laboratory, Award 70NANB14H209, through the University of Maryland.

## APPENDIX

Figures 5(a–c) shows VSM data for three stacks. The magnetic dead layer [Figs. 5(d–f)] is taken into account to calculate the saturation magnetization.

[1] I. M. Miron, K. Garello, G. Gaudin, P.-J. Zermatten, M. V. Costache, S. Auffret, S. Bandiera, B. Rodmacq, A. Schuhl, and P. Gambardella, Nature (London) **476**, 189 (2011).
[2] L. Liu, C.-F. Pai, Y. Li, H. W. Tseng, D. C. Ralph, and R. A. Buhrman, Science **336**, 555 (2012).
[3] V. E. Demidov, S. Urazhdin, H. Ulrichs, V. Tiberkevich, A. Slavin, D. Baither, G. Schmitz, and S. O. Demokritov, Nat. Mater. **11**, 1028 (2012).
[4] S. Emori, U. Bauer, S.-M. Ahn, E. Martinez, and G. S. D. Beach, Nat. Mater. **12**, 611 (2013).
[5] K.-S. Ryu, L. Thomas, S.-H. Yang, and S. Parkin, Nat. Nanotechnol. **8**, 527 (2013).
[6] W. Jiang, P. Upadhyaya, W. Zhang, G. Yu, M. B. Jungfleisch, F. Y. Fradin, J. E. Pearson, Y. Tserkovnyak, K. L. Wang, O. Heinonen, S. G. E. te Velthuis, and A. Hoffmann, Science **349**, 283 (2015).
[7] S. Woo, K. Litzius, B. Krüger, M.-Y. Im, L. Caretta, K. Richter, M. Mann, A. Krone, R. M. Reeve, M. Weigand, P. Agrawal, I. Lemesh, M.-A. Mawass, P. Fischer, M. Kläui, and G. S. D. Beach, Nat. Mater. **15**, 501 (2016).
[8] M. I. Dyakonov and V. I. Perel, Phys. Lett. **A35**, 459 (1971).
[9] J. E. Hirsch, Phys. Rev. Lett. **83**, 1834 (1999).
[10] Y. K. Kato, R. C. Myers, A. C. Gossard, and D. D. Awschalom, Science **306**, 1910 (2004).
[11] J. Wunderlich, B. Kaestner, J. Sinova, and T. Jungwirth, Phys. Rev. Lett. **94**, 047204 (2005).
[12] T. Tanaka, H. Kontani, M. Naito, T. Naito, D. S. Hirashima, K. Yamada, and J. Inoue, Phys. Rev. B **77**, 165117 (2008).
[13] H. Kontani, T. Tanaka, D. S. Hirashima, K. Yamada, and J.Inoue, Phys. Rev. Lett. **102**, 016601 (2009).
[14] U. H. Pi, K. W. Kim, J. Y. Bae, S. C. Lee, Y. J. Cho, K. S. Kim, and S. Seo, Appl. Phys. Lett. **97**, 162507 (2010).
[15] X. Wang and A. Manchon, Phys. Rev. Lett. **108**, 117201 (2012).
[16] K.-W. Kim, S.-M. Seo, J. Ryu, K.-J. Lee, and H.-W. Lee, Phys. Rev. B **85**, 180404(R) (2012).
[17] D. A. Pesin and A. H. MacDonald, Phys. Rev. B **86**, 014416 (2012).
[18] E. van der Bijl and R. A. Duine, Phys. Rev. B **86**, 094406 (2012).
[19] P. M. Haney, H.-W. Lee, K.-J. Lee, A. Manchon, and M. D. Stiles, Phys. Rev. B **87**, 174411 (2013).
[20] K.-W. Kim, H.-W. Lee, K.-J. Lee, and M. D. Stiles, Phys. Rev. Lett. **111**, 216601 (2013).
[21] J. Kim, J. Sinha, M. Hayashi, M. Yamanouchi, S. Fukami, T. Suzuki, S. Mitani, and H. Ohno, Nat. Mater. **12**, 240 (2013).
[22] K. Garello, I. M. Miron, C. O. Avci, F. Freimuth, Y. Mokrousov, S. Blügel, S. Auffret, O. Boulle, G. Gaudin, and P. Gambardella, Nat. Nanotechnol. **8**, 587 (2013).
[23] X. Fan, H. Celik, J. Wu, C. Ni, K.-J. Lee, V. O. Lorenz, and J. Q. Xiao, Nat. Commun. **5**, 3042 (2014).
[24] F. Freimuth, S. Blügel, and Y. Mokrousov, Phys. Rev. B **90** 174423 (2014).

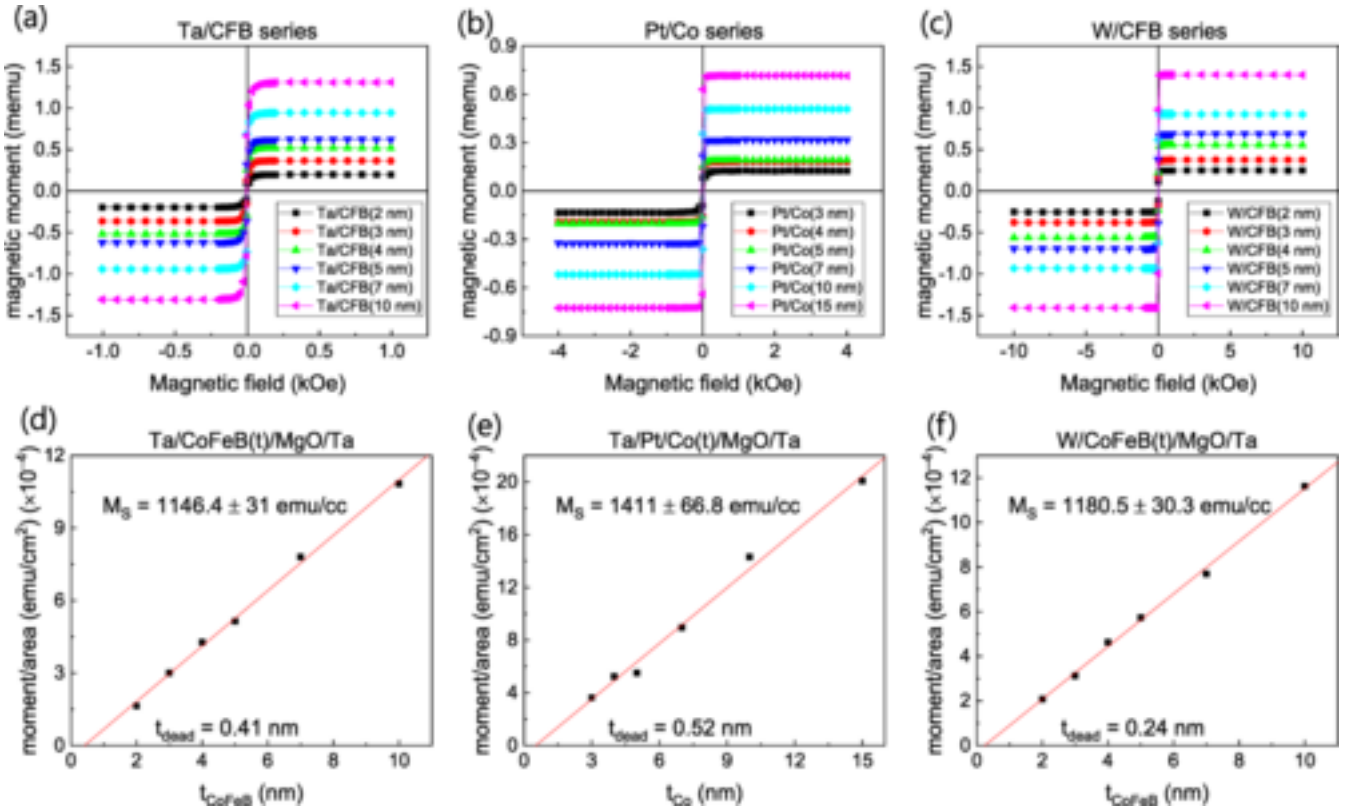


FIG. 5. (color online) VSM data: (a) Ta/CoFeB, (b) Pt/Co, and (c) W/CoFeB samples. Magnetic moment versus ferromagnet thickness: (d) Ta/CoFeB, (e) Pt/Co, and (f) W/CoFeB samples.


[25] K.-W. Kim, K.-J. Lee, H.-W. Lee, and M. D. Stiles, Phys. Rev. B **92**, 224426 (2015).

[26] X. Qiu, K. Narayanapillai, Y. Wu, P. Deorani, D.-H. Yang, W.-S. Noh, J.-H. Park, K.-J. Lee, H.-W. Lee, and H. Yang, Nat. Nanotechnol. **10**, 333 (2015).

[27] T. Taniguchi, J. Grollier, and M. D. Stiles, Phys. Rev. Appl. **3**, 044001 (2015).

[28] K.-U. Demasius, T. Phung, W. Zhang, B. P. Hughes, S.-H. Yang, A. Kellock, W. Han, A. Pushp, and S. S. P. Parkin, Nat. Commun. **7**, 10644 (2016).

[29] V. P. Amin and M. D. Stiles, Phys. Rev. B **94**, 104419 (2016).

[30] V. P. Amin and M. D. Stiles, Phys. Rev. B. **94**, 104420 (2016).

[31] Hamed Ben Mohamed Saidaoui and A. Manchon, Phys. Rev. Lett. **117**, 036601 (2016).

[32] K.-W. Kim, K.-J. Lee, J. Sinova, H.-W. Lee, and M. D. Stiles, Phys. Rev. B **96**, 104438 (2017).

[33] D. MacNeill, G. M. Stiehl, M. H. D. Guimaraes, R. A. Buhrman, J. Park, and D. C. Ralph, Nat. Phys. **13**, 300 (2017).

[34] S. Shi, S. Liang, Z. Zhu, K. Cai, S. D. Pollard, Y. Wang, J. Wang, Q. Wang, P. He, J. Yu, G. Eda, G. Liang, and H. Yang, Nat. Nanotechnol. **14**, 945 (2019).

[35] L. Liu, C. Zhou, X. Shu, C. Li, T. Zhao, W. Lin, J. Deng, Q. Xie, S. Chen, J. Zhou, R. Guo, H. Wang, J. Yu, S. Shi, P. Yang, S. Pennycook, A. Manchon, and J. Chen, Nat. Nanotechnol. **16**, 277 (2021).

[36] A. Roy, M. H. D. Guimarães, and J. S lawińska, Phys. Rev. Mater. **6**, 045004 (2022).

[37] A. M. Humphries, T. Wang, E. R. J. Edwards, S. R. Allen, J. M. Shaw, H. T. Nembach, J. Q. Xiao, T. J. Silva, and X. Fan, Nat. Commun. **8**, 911 (2017).

[38] S.-h. C. Baek, V. P. Amin, Y.-W. Oh, G. Go, S.-J. Lee, G.-H. Lee, K.-J. Kim, M. D. Stiles, B.-G. Park, and K.-J. Lee, Nat. Mater. **17**, 509 (2018).

[39] V. P. Amin, J. Zemen, and M. D. Stiles, Phys. Rev. Lett. **121**, 136805 (2018).

[40] J. Ryu, R. Thompson, J. Y. Park, S.-J. Kim, G. Choi, J. Kang, H. B. Jeong, M. Kohda, J. M. Yuk, J. Nitta, K.-J. Lee, and B.-G. Park, Nat. Electron. **5**, 217 (2022).

[41] D. Go, D. Jo, C. Kim, and H.-W. Lee, Phys. Rev. Lett. **121**, 086602 (2018).

[42] S. Iihama, T. Taniguchi, K. Yakushiji, A. Fukushima, Y. Shiota, S. Tsunegi, R. Hiramatsu, S. Yuasa, Y. Suzuki, and H. Kubota, Nat. Electron. **1**, 120 (2018).

[43] W. Wang, T. Wang, V. P. Amin, Y. Wang, A. Radhakrishnan, A. Davidson, S. R. Allen, T. J. Silva, H. Ohldag, D. Balzar, B. L. Zink, P. M. Haney, J. Q. Xiao, D. G. Cahill, V. O. Lorenz, and X. Fan, Nat. Nanotechnol. **14**, 819 (2019).

[44] V. P. Amin, Junwen Li, M. D. Stiles, and P. M. Haney, Phys. Rev. B **99**, 220405(R) (2019).

[45] J. Yu, D. Bang, R. Mishra, R. Ramaswamy, J. H. Oh, H.-J. Park, Y. Jeong, P. V. Thach, D.-K. Lee, G. Go, S.-W. Lee, Y. Wang, S. Shi, X. Qiu, H. Awano, K.-J. Lee, and H. Yang, Nat. Mater. **18**, 29 (2019).

[46] E.-S. Park, B.-C. Min, H. C. Koo, K.-W. Kim, and K.-J. Lee, Curr. Appl. Phys. **19**, 1362 (2019).

[47] K. D. Belashchenko, A. A. Kovalev, and M. van Schilfgaarde, Phys. Rev. Materials **3**, 011401(R) (2019).

[48] V. P. Amin, P. M. Haney, and M. D. Stiles, J. Appl. Phys. **128**, 151101 (2020).

[49] D. Go, F. Freimuth, J.-P. Hanke, F. Xue, O. Gomonay, K.-J. Lee, S. Blügel, P. M. Haney, H.-W. Lee, and Y. Mokrousov, Phys. Rev. Research **2**, 033401 (2020).

[50] C. Safranski, J. Z. Sun, J.-W. Xu, and A. D. Kent, Phys. Rev. Lett. **124**, 197204 (2020).

[51] K.-W. Kim and K.-J. Lee, Phys. Rev. Lett. **125**, 207205 (2020).

[52] L. Zhu, D. C. Ralph, and R. A. Buhrman, Phys. Rev. Applied **15**, 024059 (2021).

[53] E.-S. Park, D. J. Lee, O. J. Lee, B.-C. Min, H. C. Koo, K.-W. Kim, and K.-J. Lee, Phys. Rev. B **103**, 134405 (2021).

[54] S.-W. Lee and K.-J. Lee, Proc. IEEE **104**, 1834 (2016).

[55] K.-S. Lee, S.-W. Lee, B.-C. Min, and K.-J. Lee, Appl. Phys. Lett. **102**, 112410 (2013).

[56] K. Garello, C. O. Avci, I. M. Miron, M. Baumgartner, A. Ghosh, S. Auffret, O. Boulle, G. Gaudin, and P. Gambardella, Appl. Phys. Lett. **105**, 212402 (2014).

[57] K.-S. Lee, S.-W. Lee, B.-C. Min, and K.-J. Lee, Appl. Phys. Lett. **104**, 072413 (2014).

[58] G. Yu, P. Upadhyaya, Y. Fan, J. G. Alzate, W. Jiang, K. L. Wong, S. Takei, S. A. Bender, L.-T. Chang, Y. Jiang, M. Lang, J. Tang, Y. Wang, Y. Tserkovnyak, P. K. Amiri, and K. L. Wang, Nat. Nanotech. **9**, 548 (2014).

[59] S.-W. Lee and K.-J. Lee, J. Kor. Phys. Soc. **67**, 1848 (2015).

[60] T. Taniguchi, S. Mitani, and M. Hayashi, Phys. Rev. B **92**, 024428 (2015).

[61] S. Fukami, C. Zhang, S. DuttaGupta, A. Kurenkov, and H. Ohno, Nat. Mater. **15**, 535 (2016).

[62] Y.-W. Oh, S.-h. C. Baek, Y. M. Kim, H. Y. Lee, K.-D. Lee, C.-G. Yang, E.-S. Park,. K.-S. Lee, K.-W. Kim, G. Go, J.-R. Jeong, B.-C. Min, H.-W. Lee, K.-J. Lee, and B.-G. Park, Nat. Nanotech. **11**, 878 (2016).

[63] S. Fukami, T. Anekawa, C. Zhang, and H. Ohno, Nat. Nanotechnol. **11**, 621 (2016).

[64] M. Cubukcu, O. Boulle, N. Mikuszeit, C. Hamelin, T. Brächer, N. Lamard, M.-C. Cyrille, L. Buda-Prejbeanu, K. Garello, I. M. Miron, O. Klein, G. de Loubens, V. V. Naletov, J. Langer, B. Ocker, P. Gambardella, and G. Gaudin, IEEE Trans. Magn. **54**, 9300204 (2018).

[65] S.-h. C. Baek, K.-W. Park, D.-S. Kil, Y. Jang, J. Park, K.-J. Lee, B.-G. Park, Nat. Electron. **1**, 398 (2018).

[66] K. Garello, F. Yasin, S. Couet, L. Souriau, J. Swerts, S. Rao, S. Van Beek, W. Kim, E. Liu, S. Kundu, D. Tsvetanova, K. Croes, N. Jossart, E. Grimaldi, M. Baumgartner, D. Crotti, A. Fumemont, P. Gambardella, and G. S. Kar, IEEE Symposium on VLSI Circuits 81 (2018).

[67] C. Safranski, E. A. Montoya, and I. N. Krivorotov, Nat. Nanotechnol. **14**, 27 (2019).

[68] J. Ryu, S. Lee, K.-J. Lee, and B.-G. Park, Adv. Mater. **32**, 1907148 (2020).

[69] D.-K. Lee and K.-J. Lee, Sci. Rep. **10**, 1772 (2020).

[70] E. Grimaldi, V. Krizakova, G. Sala, F. Yasin, S. Couet, G. S. Kar, K. Garello, and P. Gambardella, Nat. Nanotechnol. **15**, 111 (2020).

[71] H. C. Koo, S. B. Kim, H. Kim, T.-E. Park, J. W. Choi, K.-W. Kim, G. Go, J. H. Oh, D.-K. Lee, E.-S. Park, I.-S. Hong, and K.-J. Lee, Adv. Mater. **32**, 2002117 (2020).

[72] B. Dieny, I. L. Prejbeanu, K. Garello, P. Gambardella, P. Freitas, R. Lehndorff, W. Raberg, U. Ebels, S. O. Demokritov, J. Akerman, A. Deac, P. Pirro, C. Adelmann, A. Anane, A. V. Chumak, A. Hirohata, S. Mangin, S. O. Valenzuela, M. C. Onbaşli, M. d'Aquino, G. Prenat, G. Finocchio, L. Lopez-Diaz, R. Chantrell, O. Chubykalo-Fesenko, and P. Bortolotti, Nat. Electron. **3**, 446 (2020).

[73] C. O. Avci, K. Garello, M. Gabureac, A. Ghosh, A. Fuhrer, S. F. Alvarado, and P. Gambardella, Phys. Rev. B **90**, 224427 (2014).

[74] Y.-C. Lau and M. Hayashi, Jpn. J. Appl. Phys. **56**, 0802B5 (2017).

[75] Y. Takeuchi, C. Zhang, A. Okada, H. Sato, S. Fukami, and H. Ohno, Appl. Phys. Lett. **112**, 192408 (2018).

[76] M. Li, Y.-P. Zhao, and G.-C. Wang, J. Vac. Sci. Technol. A **18**, 2992 (2000).

[77] X. Li, S.-J. Lin, M. DC, Y.-C. Liao, C. Yao, A. Naeemi, W. Tsai, and S. X. Wang, IEEE J. Electron Devices Soc. **8**, 674–680 (2020).